



HAL
open science

Enhanced Oxygen Evolution Reaction Activity of Nanoporous SnO₂/Fe₂O₃/IrO₂ Thin Film Composite Electrodes with Ultralow Noble Metal Loading

Sandra Haschke, Ying Zhuo, Stefanie Schlicht, Maïssa Barr, Ricarda Kloth, Maxime Dufond, Lionel Santinacci, Julien Bachmann

► **To cite this version:**

Sandra Haschke, Ying Zhuo, Stefanie Schlicht, Maïssa Barr, Ricarda Kloth, et al.. Enhanced Oxygen Evolution Reaction Activity of Nanoporous SnO₂/Fe₂O₃/IrO₂ Thin Film Composite Electrodes with Ultralow Noble Metal Loading. *Advanced Materials Interfaces*, 2019, 6 (3), pp.1801432. 10.1002/admi.201801432 . hal-02024335

HAL Id: hal-02024335

<https://amu.hal.science/hal-02024335v1>

Submitted on 19 Feb 2019

HAL is a multi-disciplinary open access archive for the deposit and dissemination of scientific research documents, whether they are published or not. The documents may come from teaching and research institutions in France or abroad, or from public or private research centers.

L'archive ouverte pluridisciplinaire **HAL**, est destinée au dépôt et à la diffusion de documents scientifiques de niveau recherche, publiés ou non, émanant des établissements d'enseignement et de recherche français ou étrangers, des laboratoires publics ou privés.



Distributed under a Creative Commons Attribution 4.0 International License

Enhanced Oxygen Evolution Reaction Activity of Nanoporous SnO₂/Fe₂O₃/IrO₂ Thin Film Composite Electrodes with Ultralow Noble Metal Loading

Sandra Haschke, Ying Zhuo, Stefanie Schlicht, Maïssa K. S. Barr, Ricarda Kloth, Maxime E. Dufond, Lionel Santinacci, and Julien Bachmann*

A conductive SnO₂ layer and small quantities of IrO₂ surface cocatalyst enhance the catalytic efficiency of nanoporous Fe₂O₃ electrodes in the oxygen evolution reaction at neutral pH. Anodic alumina templates are therefore coated with thin layers of SnO₂, Fe₂O₃, and IrO₂ by atomic layer deposition. In the first step, the Fe₂O₃ electrode is modified with a conductive SnO₂ layer and submitted to different postdeposition thermal treatments in order to maximize its catalytic performance. The combination of steady-state electrolysis, electrochemical impedance spectroscopy, X-ray crystallography, and X-ray photoelectron spectroscopy demonstrates that catalytic turnover and e⁻ extraction are most efficient if both layers are amorphous in nature. In the second step, small quantities of IrO₂ with extremely low iridium loading of 7.5 μg cm⁻² are coated on the electrode surface. These electrodes reveal favorable long-term stability over at least 15 h and achieve maximized steady-state current densities of 0.57 ± 0.05 mA cm⁻² at η = 0.38 V and pH 7 (1.36 ± 0.10 mA cm⁻² at η = 0.48 V) in dark conditions. This architecture enables charge carrier separation and reduces the photoelectrochemical water oxidation onset by 300 mV with respect to pure Fe₂O₃ electrodes of identical geometry.

1. Introduction


To reach the global goal of an ample, sustainable, and carbon-free energy production, the efficient use of renewable energy

S. Haschke, Y. Zhuo, S. Schlicht, Dr. M. K. S. Barr, R. Kloth, Prof. J. Bachmann
Chemistry of Thin Film Materials
Department of Chemistry and Pharmacy
Friedrich-Alexander University Erlangen-Nürnberg
Egerlandstraße 1, 91058 Erlangen, Germany
E-mail: julien.bachmann@fau.de

M. E. Dufond, Dr. L. Santinacci
CINAM
CNRS

Aix Marseille Université
13288 Marseille, France

Prof. J. Bachmann
Institute of Chemistry
Saint-Petersburg State University
Universitetskii pr. 26, 198504 St. Petersburg, Russia

 The ORCID identification number(s) for the author(s) of this article can be found under <https://doi.org/10.1002/admi.201801432>.

DOI: 10.1002/admi.201801432

sources is inalienable. Among renewable energy resources, the sun is the most striking candidate with its capability of satisfying the world's annual total energy consumption with less than an hour of solar energy.^[1] However, solar energy utilization faces a major challenge in addition to the efficient capture and conversion of solar radiation itself, namely, the storage and transportation of the energy produced.^[1,2] This latter aspect can be integrated into the former in the form of the photoelectrochemical (PEC) splitting of water into dioxygen and dihydrogen. This reaction offers the possibility to convert and store solar energy in form of chemical bonds directly.^[3] Here, the oxidation of H₂O to O₂ has proven to be the more demanding half-reaction.^[4] Among a great variety of suitable photoanode materials, iron oxide (Fe₂O₃) stands out as an abundant and inexpensive potential semiconductor and catalyst.^[5] Fe₂O₃ also offers a favorable

bandgap of 2.0–2.2 eV,^[6] a valence band energy position sufficiently positive for the water oxidation reaction (2.4–2.7 V vs normal hydrogen electrode (NHE)),^[7] and chemical stability in neutral and moderately basic pH.^[6c,8] However, its slow oxygen evolution kinetics,^[9] poor electrical conductivity (σ ≈ 10⁻¹² Ω⁻¹ m⁻¹),^[10] relatively large light absorption depth (α⁻¹ = 118 nm for a wavelength of λ = 550 nm),^[11] short hole diffusion length (2–4 nm),^[6c,12] and its correlated high rate of charge carrier recombination^[9,13] limit the PEC anode efficiency.

Among the diverse approaches that have been applied to overcome these drawbacks, we will focus on the following three. 1) Efforts to *nanostructure* photoanodes and simultaneously reduce the iron oxide thickness have improved the water oxidation performance.^[13a,14] Porosity in a macroscopically thick Fe₂O₃ layer enhances light collection while each individual structure may be microscopically thin in order to balance the development of an electrostatic field (depletion region) with a short charge carrier collection distance.^[15] 2) Enhanced efficiencies can also be achieved by introducing a *conductive scaffold* that collects and transports the photoexcited electrons and thereby avoids charge carrier recombination.^[15d,16] 3) Fe₂O₃ surfaces can be further modified with a particularly proficient water oxidation *cocatalyst*.^[17] The lower kinetic barrier of the cocatalyst

facilitates an alternative pathway for the oxygen evolution reaction (OER). The fast consumption of holes by the chemical reaction minimizes their accumulation at the solid–liquid interface, and thereby their recombination with majority charge carriers.^[17a]

Herein, we report a nanoporous SnO₂/Fe₂O₃/IrO₂ thin film composite electrode with extremely low noble metal loading prepared by atomic layer deposition (ALD) for the OER under favorable benign (pH neutral) conditions. ALD is chosen as the deposition method due to its ability to conformally coat high aspect ratio substrates (anodic alumina) with precisely defined film thicknesses. The transparent SnO₂ with its slightly lower conduction band energy^[18] and sufficient conductivity (at least 10¹¹ times higher than $\sigma(\text{Fe}_2\text{O}_3)$)^[19] fulfills the requirements for an electron collector. IrO₂, as one of the most active OER catalyst materials, is ideal as the cocatalyst on the surface.^[20] We will proceed in two steps. At first, a conductive SnO₂ layer is added to the nanoporous Fe₂O₃ electrode and the system is characterized with respect to its morphology and phase composition. Since the crystallinity of the individual layers strongly influences their electronic properties, postdeposition thermal treatments are applied to the SnO₂/Fe₂O₃ electrode. In the second step, the optimized SnO₂/Fe₂O₃ electrode is additionally coated with small quantities of IrO₂ cocatalyst. These anodes reveal extremely low noble metal loadings of 7.5 $\mu\text{g cm}^{-2}$ (standard OER loading: >1 mg cm^{-2})^[21] and favorable long-term stability under neutral conditions. In the dark, they achieve maximized steady-state current densities of $0.57 \pm 0.05 \text{ mA cm}^{-2}$ at 0.38 V applied overpotential. Furthermore, the combination of the SnO₂ conductive layer and IrO₂ cocatalyst successfully separates photogenerated charge carriers, causing a shift of 300 mV to lower *E* with respect to pure Fe₂O₃ electrodes.

2. Results and Discussion

2.1. Nanoporous SnO₂/Fe₂O₃ Composite Electrodes

The type of nanoporous iron oxide electrodes optimized in earlier studies^[22] will first be modified with a conductive SnO₂ layer. The preparation starts with an ordered array of parallel, cylindrical “anodic” Al₂O₃ pores of $\approx 370 \text{ nm}$ diameter (*D*) and 11 μm length (*L*) as the electrode template (see Figure S1, steps (a)–(e), in the Supporting Information). This template is functionalized with a micrometer-thick electrical Ni backside contact by sputter coating 100 nm of Au followed by galvanic deposition of Ni. The high aspect ratio substrate is subsequently coated with $\approx 20 \text{ nm}$ of SnO₂^[23] followed by 10 nm of Fe₂O₃^[22b,c] via ALD. Scanning electron microscopy (SEM) images of an as-prepared electrode in top and cross-sectional views (Figure 1a,b) show the periodic arrangement of well-defined pores equipped with the Ni backside contact at the pore extremities (including $\approx 1 \mu\text{m}$ long Ni segments in the pores). The presence of Fe and Sn on the alumina template can be proven by energy-dispersive X-ray spectroscopy (EDX) element analysis (Figure 1c). EDX profiles recorded along the pores’ depth demonstrate that ALD is the suitable tool to coat the porous substrate with thin, continuous layers of SnO₂ and Fe₂O₃ (Figure 1d).

The chemical identity of the two individual layers is provided by X-ray photoelectron spectroscopy (XPS, Figure 2). The

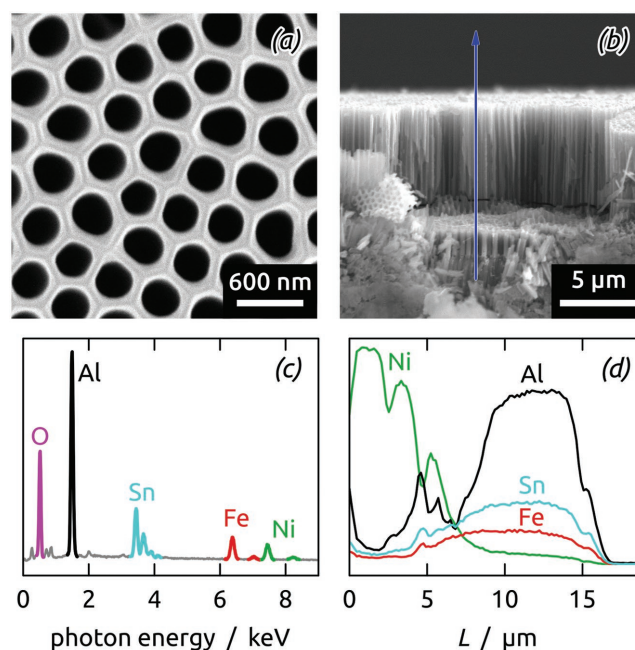


Figure 1. SEM images of a nanoporous SnO₂/Fe₂O₃ electrode after all preparation steps in a) top view and b) cross section. c) EDX spectrum recorded from the top of the sample. d) EDX profile taken along the cross section. SnO₂ and Fe₂O₃ are present homogeneously along the pores.

overview XPS spectrum of the nanoporous SnO₂-coated sample (Figure 2a) features only Sn, O, and C, whereas the Al₂O₃ template is homogeneously covered and generates no Al signal. Deconvolution of the Sn 3d region (Figure 2b) reveals two peaks at 487.1 and 495.5 eV, which are consistent with Sn(IV) in SnO₂.^[23,24] This assignment is confirmed by the deconvoluted O 1s peak centered at 531.0 eV (Figure 2c).^[23,24b] Contributions at higher binding energies can be ascribed to adsorbed oxygen or the presence of water.^[23] After the deposition of the catalyst layer, conspicuous Fe peaks arise in the overview survey, whereas the Sn 3d signal almost vanishes (Figure 2a). This observation is reasonable since the iron oxide thickness is in the range of the average XPS analysis depth of 10 nm. The binding energies of 710.7, 724.2, and 529.8 eV for the Fe 2p_{3/2} and 2p_{1/2} and O 1s peaks, respectively, correspond to Fe(III) in Fe₂O₃ (Figure 2c,d).^[22b,25] The nature of the conductive SnO₂ layer remains unchanged with a marginal Sn 3d and O 1s peak shift to lower binding energies (Figure 2b,c). Furthermore, both layers are of amorphous nature since the X-ray diffraction (XRD) pattern (Figure 3) only features peaks of the crystalline Al template frame (Crystallographic Open Database, COD 9008460) and Au/Ni electrical contact (COD 1100138 and COD 2100649).

Since the crystallinity of the individual layers is often crucial for their functional performance,^[15d,22c,26] thermal treatments are applied to the SnO₂ and Fe₂O₃ layers with the objective of maximized catalytic turnover in the OER. Annealing (400 °C, N₂) of the conductive layer on its own provides crystalline cassiterite (SnO₂, COD 1000062), which subsequently results in a partially crystalline hematite (α -Fe₂O₃, COD 5910082) film growth upon ALD (Figure 3). In contrast to that, annealing both

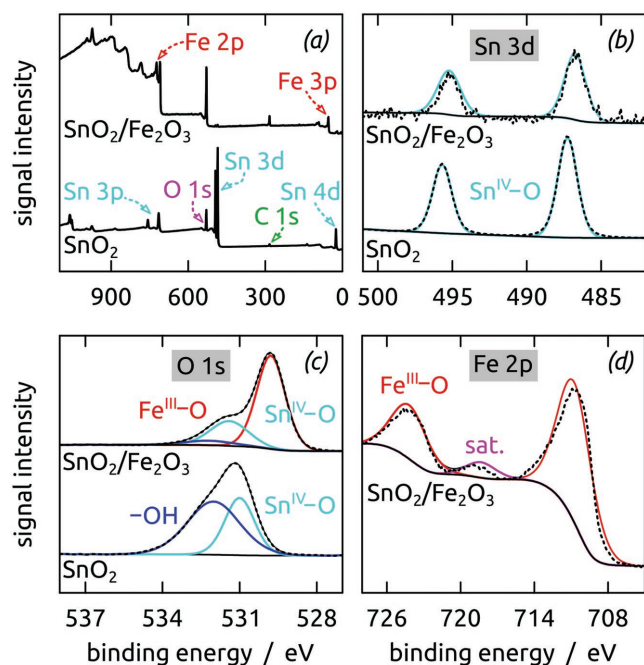


Figure 2. X-ray photoelectron spectra of the nanoporous SnO₂-coated template and the corresponding SnO₂/Fe₂O₃ composite electrode. All spectra are shifted to a C 1s binding energy of 284.8 eV. a) The survey spectra show the expected elements. Deconvolution of the core level spectra of b) Sn 3d, c) O 1s, and d) Fe 2p proves the SnO₂ and Fe₂O₃ chemical identities. The experimental data are provided as dashed lines, the fits as solid black lines, and the individual deconvoluted peaks are color coded.

layers together (we will call this case “the SnO₂/Fe₂O₃ electrode annealed postdeposition”) results in pronounced crystalline cassiterite and hematite signals in the XRD pattern.

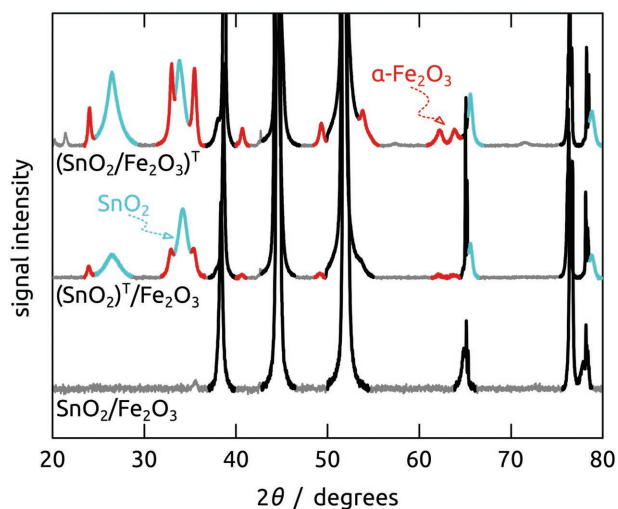


Figure 3. X-ray diffraction pattern of as-deposited and annealed SnO₂/Fe₂O₃ electrodes. A comparison is drawn between an as-deposited SnO₂/Fe₂O₃ electrode, an electrode with SnO₂ annealed on its own, (SnO₂)^T/Fe₂O₃, and an electrode annealed after the deposition of both layers, (SnO₂/Fe₂O₃)^T. The signals corresponding to the Al frame (COD 9008460) and Au/Ni contact (COD 1100138, COD 2100649) are shown in black. The crystalline peaks of SnO₂ (COD 1000062) and α-Fe₂O₃ (COD 5910082) are highlighted in cyan and red, respectively.

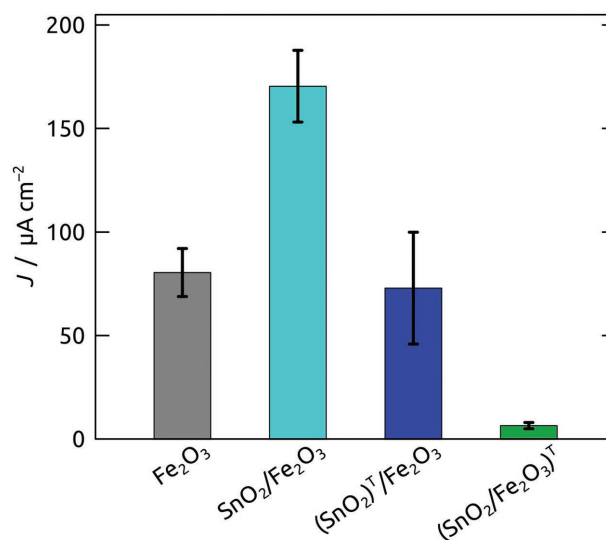


Figure 4. Steady-state current densities of nanoporous SnO₂/Fe₂O₃ electrodes for water oxidation at pH 7 (0.1 M KH₂PO₄ electrolyte) and +1.10 V vs Ag/AgCl ($\eta = 0.48$ V). Comparison is drawn between the pure Fe₂O₃ electrode,^[22c] the as-deposited SnO₂/Fe₂O₃ electrode (cyan bar), the composite electrode with annealed SnO₂ (blue bar), and the electrode annealed postdeposition (green bar). The error bars correspond to the values determined for at least three nominally identical individual samples.

The water oxidation performance of these differently treated electrodes is now studied by a combination of steady-state electrolysis (**Figure 4**) and electrochemical impedance spectroscopy (EIS, **Figure 5**) at $E = +1.10$ V vs Ag/AgCl (overpotential $\eta = 0.48$ V) in neutral pH conditions. All three types of electrodes show two semicircles in the Nyquist plots (Figure 5a,b). The corresponding model (Figure 5c) therefore considers two interfaces, the liquid–solid and the solid–solid interface, each of them consisting of a charge-transfer resistance (R) and a non-ideal capacitor (Q). For the interpretation of the OER activity, both resistances $R_{l/s}$ and $R_{s/s}$ are of physical–chemical significance since they are directly related to the inherent catalytic activity and to the ability of electron (e^-) extraction (see Table S1 in the Supporting Information). The as-deposited amorphous SnO₂/Fe₂O₃ electrodes yield the lowest $R_{s/s}$ and $R_{l/s}$ values of 7 and 182 Ω cm⁻², as well as the highest current densities $J = 171 \pm 17$ μ A cm⁻² (the uncertainty stated here refers to measurements performed on at least three nominally identical individual samples). The doubling of J relative to the pure nanoporous Fe₂O₃ electrode^[22c] proves the suitability of amorphous SnO₂ for efficient e^- extraction. Notably, any catalytic contributions of SnO₂ can be excluded by a control experiment ($J = 0.3 \pm 0.3$ μ A cm⁻²). Thermal treatment of the conductive layer, however, reveals lower current densities and, additionally, an increase in $R_{s/s}$ and $R_{l/s}$ with respect to the as-deposited SnO₂/Fe₂O₃ electrode. This deterioration demonstrates that, first, the crystalline SnO₂ loses its function as a conductive layer and, second, the commencing crystallization of Fe₂O₃ reduces its catalytic activity. This trend is even more pronounced for the electrodes annealed postdeposition with crystalline SnO₂ and Fe₂O₃. Here, $R_{s/s}$ and $R_{l/s}$ are ≈ 1.8 and ≈ 5.2 k Ω cm⁻², indicating a mismatch of the conduction band energy positions

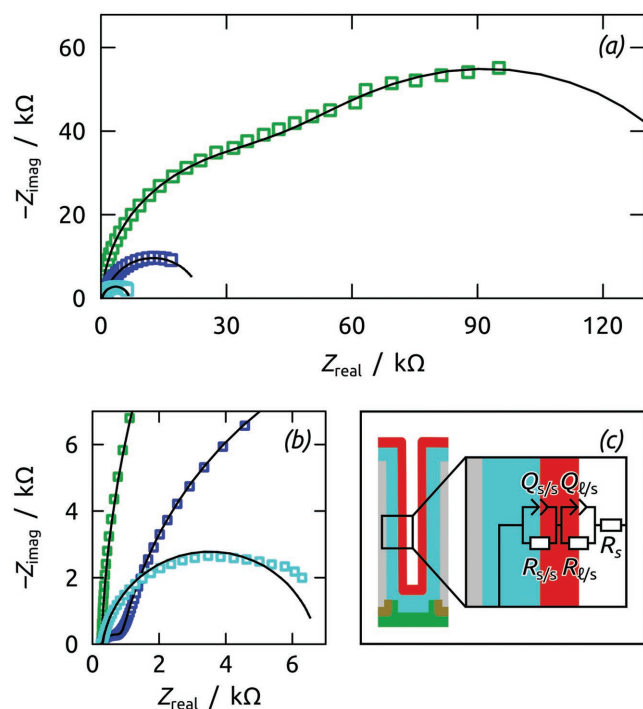


Figure 5. EIS spectra (recorded at +1.10 V vs Ag/AgCl ($\eta = 0.48$ V) in a 0.1 M KH_2PO_4 electrolyte at pH 7) of nanoporous $\text{SnO}_2/\text{Fe}_2\text{O}_3$ electrodes submitted to various thermal treatments. Nyquist plots are presented for the as-deposited $\text{SnO}_2/\text{Fe}_2\text{O}_3$ electrode (cyan squares), the composite electrode with annealed SnO_2 (blue squares), and the electrode annealed postdeposition (green squares) superimposed with fitted curves (black lines): a) overall and b) in a zoom. c) The equivalent circuit model consists of a series resistance (R_s), a charge-transfer resistance ($R_{l/s}$), and a nonideal capacitor (constant-phase element) ($Q_{l/s}$) for the liquid–solid interface, and a charge-transfer resistance ($R_{s/s}$) and nonideal capacitor ($Q_{s/s}$) for the solid–solid interface.

and a strongly reduced catalytic activity of crystalline Fe_2O_3 . The lower water oxidation efficiency of crystalline Fe_2O_3 is in line with earlier studies on nanoporous Fe_2O_3 electrodes.^[22c] In summary, the amorphous nature of the as-deposited nanoporous $\text{SnO}_2/\text{Fe}_2\text{O}_3$ composite electrode proves to be ideal for a maximized OER activity. This electrode architecture represents the basis for subsequent electrode modification.

2.2. Nanoporous $\text{SnO}_2/\text{Fe}_2\text{O}_3/\text{IrO}_2$ Composite Electrodes

In the second part, an IrO_2 cocatalyst is applied to the optimized nanoporous $\text{SnO}_2/\text{Fe}_2\text{O}_3$ electrode. However, the introduction of the low-abundance and expensive IrO_2 requires the minimization of its loading. Therefore, only seven ALD cycles of iridium oxide (significantly less than 1 nm)^[27] are deposited on top of the nanoporous $\text{SnO}_2/\text{Fe}_2\text{O}_3$ electrode (step (f) in Figure S1, Supporting Information). The successful deposition is demonstrated by EDX (Figure S2, Supporting Information) and XPS (Figure 6). This very low IrO_2 loading is, however, not observable in transmission electron microscopy (TEM, Figure S3, Supporting Information). The analysis of the XPS survey (Figure 6a) shows the presence of Ir, O, Fe, and C, whereas Sn is not detectable any longer. The Fe 2p peaks

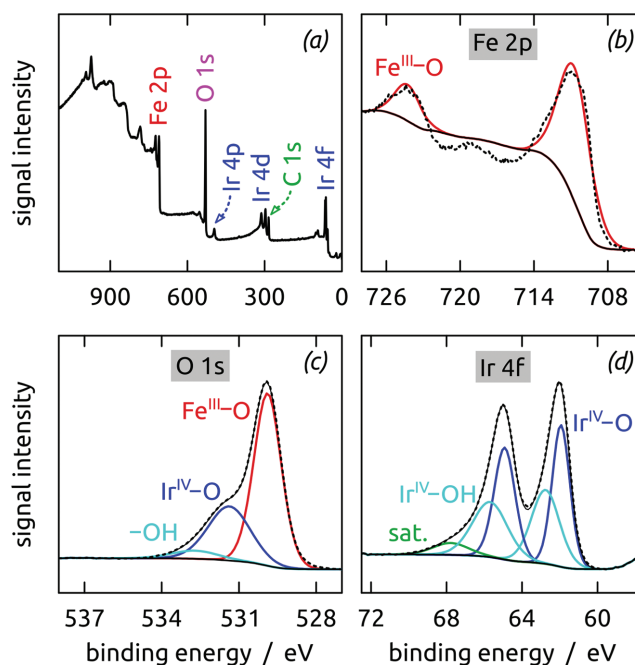


Figure 6. X-ray photoelectron spectra of the nanoporous $\text{SnO}_2/\text{Fe}_2\text{O}_3/\text{IrO}_2$ composite electrode. All spectra are shifted to a C 1s binding energy of 284.8 eV. a) The survey spectra show the expected elements. Deconvolution of the core level spectra of b) Fe 2p, c) O 1s, and d) Ir 4f identifies the presence of Fe_2O_3 and partly hydrated Ir(IV) oxide. The experimental data are provided as dashed lines, the fits as solid black lines, and the individual deconvoluted peaks are color coded.

and thus the iron oxide chemical identity remain unchanged upon cocatalyst coating (Figure 6b,c). Deconvolution of the Ir 4f region reveals two doublets for two chemically distinct Ir environments (Figure 6d). Their Ir $4f_{7/2}$ maxima centered at 61.9 and 62.7 eV are consistent with IrO_2 and hydrated Ir(IV) oxide, respectively.^[28] This observation is also confirmed by the O 1s region (Figure 6c). Furthermore, the seven cycles of IrO_2 coating correspond to an ultralow iridium loading of $7.5 \mu\text{g cm}^{-2}$ as quantified by inductively coupled plasma optical emission spectrometry (ICP-OES).

To quantify the effectiveness of the nanoporous $\text{SnO}_2/\text{Fe}_2\text{O}_3/\text{IrO}_2$ electrodes in the OER, the steady-state current densities are compared to those of pure Fe_2O_3 , $\text{SnO}_2/\text{Fe}_2\text{O}_3$, and $\text{Fe}_2\text{O}_3/\text{IrO}_2$ electrodes (Figure 7). At an applied overpotential of $\eta = 0.48$ V, $\text{SnO}_2/\text{Fe}_2\text{O}_3/\text{IrO}_2$ electrodes achieve $1.36 \pm 0.10 \text{ mA cm}^{-2}$ (Figure 7a). This value corresponds to a J improvement by factors of 8 and 17 with respect to $\text{SnO}_2/\text{Fe}_2\text{O}_3$ and pure Fe_2O_3 electrodes, respectively. In contrast to that, the application of an IrO_2 coating on the as-deposited Fe_2O_3 electrode only yields $0.11 \pm 0.02 \text{ mA cm}^{-2}$ even with ten ALD cycles. Control experiments with $\text{SnO}_2/\text{IrO}_2$ electrodes ($J = 0.01 \pm 0.01 \text{ mA cm}^{-2}$) additionally prove the need for the three-layer architecture. Any contributions of the nickel electrical contact to the overall J are small ($J = 0.03 \text{ mA cm}^{-2}$ from our control experiments) and therefore negligible. The effect of ozone treatment on the Fe_2O_3 surface upon IrO_2 deposition cannot be the cause for the performance improvement, since Fe_2O_3 is also deposited with O_3 at almost the same temperature. Even more convincing is the $\text{SnO}_2/\text{Fe}_2\text{O}_3/\text{IrO}_2$ electrode performance at lower η shown in

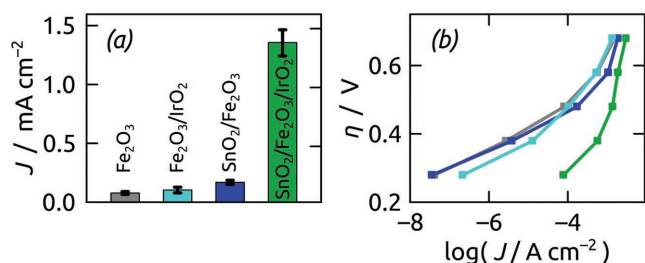


Figure 7. Steady-state water oxidation performance of as-deposited and modified nanoporous Fe_2O_3 electrodes recorded in a $0.1 \text{ M KH}_2\text{PO}_4$ electrolyte at pH 7. a) Current densities measured at an applied overpotential of $\eta = 0.48 \text{ V}$ ($+1.1 \text{ V}$ vs Ag/AgCl), and b) corresponding Tafel plots of the same electrodes.

the corresponding Tafel plot (Figure 7b). Reducing η to 0.38 V still yields $0.57 \pm 0.05 \text{ mA cm}^{-2}$ —a 188-fold improvement relative to pure Fe_2O_3 . At $\eta = 0.28 \text{ V}$, they enable an OER turnover that exceeds those of Fe_2O_3 electrodes even by a factor of 1925, or, equivalently, 3.3 decimal logarithmic units. These electrodes additionally reveal favorable long-term stability over at least 15 h of steady-state electrolysis (Figure S4, Supporting Information) without measurable loss of the IrO_2 cocatalyst (Figure S2, Supporting Information). The nanoporous Fe_2O_3 , $\text{Fe}_2\text{O}_3/\text{IrO}_2$, and $\text{SnO}_2/\text{Fe}_2\text{O}_3$ electrodes are characterized by nonlinear Tafel plots, with slopes increasing from $60 \pm 10 \text{ mV}$ per decade at low applied overpotential ($\eta \leq 0.48 \text{ V}$) to $170 \pm 15 \text{ mV}$ per decade at $\eta \geq 0.48 \text{ V}$. In comparison, the $\text{SnO}_2/\text{Fe}_2\text{O}_3/\text{IrO}_2$ electrodes yield ≈ 150 and $\approx 580 \text{ mV}$ per decade in these two regimes, respectively. Such large values of the Tafel slopes are characteristic of an OER that is no longer limited by the catalytic turnover at the surface, but by mass/charge transport in the pores.^[27] In practical terms, they express that our nanoporous electrodes are most efficient at lower applied overpotentials.

Based on these results and the band alignment of our semiconductors (Figure 8),^[7a,29] we expect a photoelectrochemical

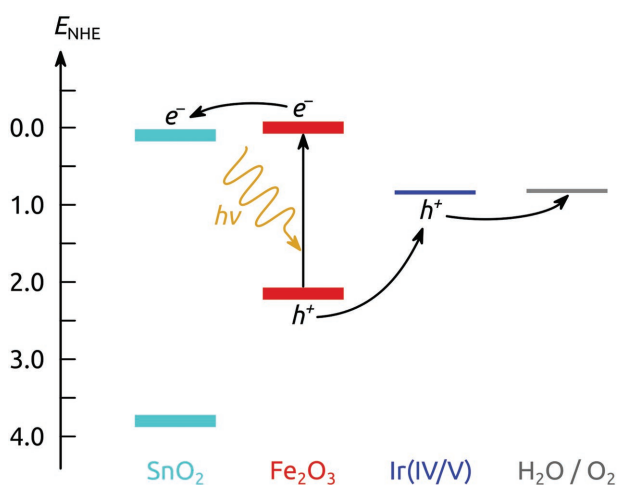


Figure 8. Schematic illustration of the energy band diagram for the photoelectrochemical oxygen evolution reaction at $\text{SnO}_2/\text{Fe}_2\text{O}_3/\text{IrO}_2$ electrodes at pH 7. The band edge positions of SnO_2 and Fe_2O_3 as well as the standard redox potentials of the catalytically active redox couple $\text{Ir}(\text{IV})/\text{Ir}(\text{V})$ and the $\text{H}_2\text{O}/\text{O}_2$ couple are indicated relative to the NHE in thick and thinner lines, respectively.^[7a,29]

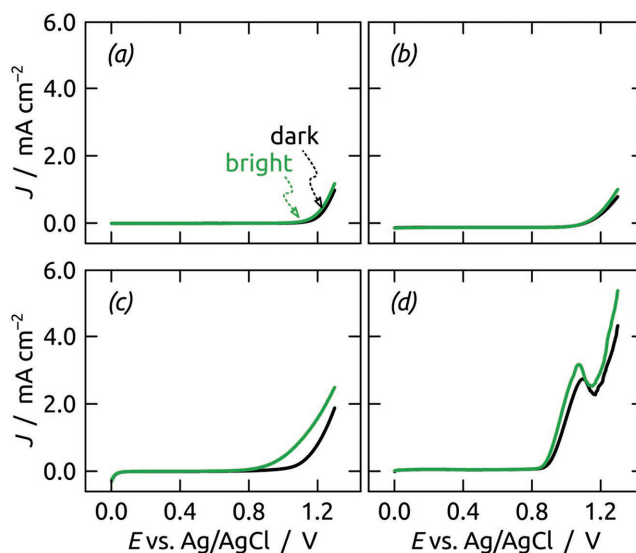


Figure 9. J - E curves of a) nanoporous Fe_2O_3 , b) $\text{Fe}_2\text{O}_3/\text{IrO}_2$, c) $\text{SnO}_2/\text{Fe}_2\text{O}_3$, and d) $\text{SnO}_2/\text{Fe}_2\text{O}_3/\text{IrO}_2$ electrodes recorded in the dark (black line) and bright (green line) simulated sunlight AM 1.5G, 100 mW cm^{-2} conditions. The curves are measured with a scan rate of 10 mV s^{-1} in a $0.1 \text{ M KH}_2\text{PO}_4$ electrolyte at pH 7.

activity upon solar irradiation. The experimental data are presented in Figure 9 and Figure S5 in the Supporting Information. The initial system, the nanoporous Fe_2O_3 electrode, only yields negligible photocurrents (Figure 9a). The lack of photoresponse probably results from both the slow water oxidation kinetics and the low semiconductor conductivity, a combination associated with predominant charge carrier recombination.^[10,15b,d] Lowering the OER kinetic barrier with the IrO_2 cocatalyst reveals no significant difference with respect to the Fe_2O_3 electrode (Figure 9b). Thus, e^- transport in the semiconductor layer must be the major limiting factor. Indeed, with SnO_2 as a conductive layer (but no IrO_2), a clear shift of $\approx 170 \text{ mV}$ (at $J = 0.2 \text{ mA cm}^{-2}$) can be observed upon illumination in the J - E curve (Figure 9c). This shift demonstrates that photoinduced e^- are efficiently extracted via the conductive SnO_2 layer. Consequently, the $\text{SnO}_2/\text{Fe}_2\text{O}_3$ photoanode performance is now limited by the OER kinetics. By adding both functional materials to one Fe_2O_3 electrode, the best PEC performance can be achieved with a shift of 300 mV to lower E (at $J = 0.2 \text{ mA cm}^{-2}$) relative to the pure Fe_2O_3 electrode (Figure 9d). In this system, e^- extraction and H_2O oxidation turnover are in fact so efficient that transport of ions in the pores becomes the limiting factor at a certain applied potential (observable as a peak at $+1.1 \text{ V}$). A rough approximation of the external photoelectrochemical quantum efficiency reached in these conditions can be obtained by comparing our current density (on the order of 0.44 mA cm^{-2} at 0.38 V overpotential for $\text{SnO}_2/\text{Fe}_2\text{O}_3$) with the solar photon flux between 2.1 eV (bandgap of Fe_2O_3)^[6] and 3.8 eV (bandgap of SnO_2),^[7a] yielding 4%.^[30] This value is lower than efficiencies reported for similar Fe_2O_3 -based electrodes (Table S2, Supporting Information).^[15d,16d,31] However, all of them are applied in strongly alkaline medium (pH 13.6), which is associated with a larger driving force from the Fe_2O_3 valence band edge (by $\approx 0.4 \text{ V}$) and thus influences charge separation favorably.

3. Conclusions

Nanoporous SnO₂/Fe₂O₃/IrO₂ thin film composite electrodes, suitable for the OER in neutral media, have been successfully prepared by atomic layer deposition. If the nanoporous Fe₂O₃ is first modified with a conductive SnO₂ layer only, efficient e⁻ extraction and maximized catalytic turnover are only achieved if both SnO₂ and Fe₂O₃ are amorphous. In contrast to that, thermal annealing crystallizes SnO₂ and Fe₂O₃ and thereby deteriorates both desired properties. Taking this knowledge as a basis, the as-deposited SnO₂/Fe₂O₃ electrodes are subsequently further modified with seven ALD cycles of IrO₂. These composite electrodes reveal extremely low noble metal loadings of 7.5 μg cm⁻² and desirable long-term stability for at least 15 h of steady-state electrolysis. In the dark, our nanoporous SnO₂/Fe₂O₃/IrO₂ electrode yields maximized steady-state current densities of 0.57 ± 0.05 mA cm⁻² at η = 0.38 V corresponding to a 188-fold improvement with respect to pure Fe₂O₃ electrodes. The reduction of η to 0.28 V even enhances the J improvement factor to a value of 1925. We want to highlight here that this performance is achieved under favorable benign (pH neutral) conditions, whereas most other Fe₂O₃ electrodes of similar architecture are applied in strongly basic conditions.^[15d,16d,17a,31,32] Using an alkaline medium also improves the performance of our Fe₂O₃-based electrodes significantly, as expected (see Figure S6 in the Supporting Information), however, at the expense of a lack of long-term stability.^[17a] In fact, our *stable* dark currents measured at η = 0.38 V in neutral media outperform those of most Fe₂O₃-based electrodes (some featuring a transparent conductive oxide scaffold and/or an IrO₂ cocatalyst coating) independent of their pH conditions (Table S3, Supporting Information).^[16d,17a,b,29a,31] Additionally, the improved catalytic turnover combined with efficient charge carrier separation allows for a significant shift in the photocurrent response by 300 mV to lower E with respect to pure Fe₂O₃ electrodes.

4. Experimental Section

Materials: Chemicals were purchased from Sigma-Aldrich, Alfa Aesar, ABCR, Strem, or VWR and used as received. Water was purified in a Millipore Direct-Q system for application in electrolytes. Aluminum plates (99.99%) and Si(100) wafers covered with an oxide layer were supplied by Smart Membranes and Silicon Materials Inc., respectively. Ozone was generated with a BMT 803N ozone generator from oxygen purchased from Air Liquide.

Preparation of Nanostructured Composite Electrodes: Nanostructured composite electrodes were prepared in a multistep procedure as illustrated in Figure S1 in the Supporting Information. First the nanoporous alumina oxide templates were obtained via the standard two-step anodization of aluminum (represented as (a) in Figure S1 in the Supporting Information).^[33] Homemade two-electrode cells consisting of a polyvinyl chloride beaker with four circular openings at the bottom were used to anodize aluminum plates of 2.2 cm diameter, which were therefore held between an O-ring and a thick copper plate operating as an electrical contact. Adequate cooling of the beaker was ensured via a cold plate connected to a closed-circuit cooler by Haake. Each beaker was filled with electrolyte and closed with a lid containing a mechanical stirrer and silver wire mesh as the counter electrode. The whole setup was thermally insulated laterally. The aluminum plates were electropolished in a cooled perchloric acid/ethanol solution (1:3 v/v HClO₄/EtOH) for 5 min under +20 V, rinsed, and cooled before

anodizing them under +195 V for 23 h at 0 °C in 1 wt% H₃PO₄. The disordered, porous Al₂O₃ generated was then removed in a chromic acid solution (0.18 M CrO₃ in 6 wt% H₃PO₄) for 23 h at 45 °C. The second anodization was subsequently performed for 4 h at 0 °C in 1 wt% H₃PO₄ yielding the well-ordered Al₂O₃ matrix. The next step involved the removal of the metallic Al on the backside of the anodized Al₂O₃ with 0.7 M CuCl₂ solution in 10% HCl, followed by opening the Al₂O₃ barrier layer closing the pores with simultaneous isotropic pore widening in 10 wt% H₃PO₄ at 45 °C for 39 min (step (b) in Figure S1, Supporting Information). The AAO template was subsequently equipped with an electrical contact at one side of pore extremities (step (c) in Figure S1, Supporting Information). To this goal, 100 nm of gold was deposited on the templates in a Torr CRC 622 sputter coater operating in DC mode for subsequent electrodeposition of a thicker nickel contact. Ni was electroplated from a diluted Watts electrolyte (0.57 M NiSO₄·6H₂O, 95 × 10⁻³ M NiCl₂·6H₂O, and 0.5 M H₃BO₃ adjusted to pH 3.0) in a two-electrode configuration with a Pt mesh as counter electrode under -2.3 V for 4 h. The final AAO templates were then coated by atomic layer deposition. The deposition of SnO₂ was performed in a commercial Gemstar-6 XT ALD reactor from Arradiance operating with N₂ as carrier gas (step (d) in Figure S1, Supporting Information). ALD was carried out at 200 °C with tetrakis(dimethylamino)tin(IV) and H₂O₂ both kept in stainless steel bottles maintained at 60 °C and room temperature, respectively. The pulse, exposure, and purge times for both precursors were 0.5, 40, and 120 s, respectively. 430 ALD cycles yielded ≈20 nm of SnO₂.^[23] Fe₂O₃ was deposited in a home-built hot-wall reactor fitted with a chemically resistant diaphragm pump MV10C from Vacuubrand (step (e) in Figure S1, Supporting Information). The ALD process was performed with N₂ as carrier gas at a chamber temperature of 200 °C. Ferrocene (Cp₂Fe, kept in a stainless steel bottle maintained at 70 °C) and ozone were used as precursors with pulse, exposure, and purge times of 2, 40, and 60, and 0.2, 40, and 60 s, respectively. 800 ALD cycles were performed in order to obtain ≈10 nm of Fe₂O₃ on the functional samples.^[22b,c] The IrO₂ deposition was carried out with ethylcyclopentadienyl-1,3-cyclohexadieneiridium(I) ((EtCp)Ir(CHD), kept at 90 °C in a stainless steel bottle) and O₃ at 220 °C in the commercial Gemstar-6 XT ALD reactor (step (f) in Figure S1, Supporting Information). Four consecutive microcycles each consisting of a 0.5 s (EtCp)Ir(CHD) pulse and 40 s of exposure time were performed before the chamber was purged with N₂ for 90 s. Ozone was introduced in a single pulse of 0.5 s, whereas exposure and purge durations were 40 and 90 s, respectively. Seven or ten macrocycles were used for the cocatalyst coatings. Approximately 10 nm of IrO₂ was deposited with 150 macrocycles for control experiments.^[27] For the determination of the Fe₂O₃, SnO₂, and IrO₂ layer thicknesses, silicon wafers coated with Al₂O₃ or indium-doped tin oxide were added to the reaction chamber and subsequently characterized by spectroscopic ellipsometry.

Annealings: Samples having undergone the complete preparative procedure were annealed in a muffle furnace from Nabertherm under N₂ atmosphere. The nanoporous samples were heated up to 400 °C over 12 h, maintained at this temperature for 4 h, and cooled down to room temperature over 12 h.

Instrumental Methods: The Fe₂O₃ and SnO₂ layer thicknesses were determined on Si(100) wafers with a Sentech spectroscopic ellipsometer SENpro equipped with a tungsten halogen lamp. 50 data points were recorded for wavelengths between 380 and 1050 nm under an angle of 70° for each measurement. The software SpectraRay/3 was used to fit the data orientation (Θ) and ellipticity (ε) with fixed optical models for Fe₂O₃ and SnO₂. SEM and EDX were carried out on a JEOL JSM 6400 PC implemented with a LaB₆ cathode and SDD X-ray detector. Further SEM images and EDX spectra were recorded with a Zeiss EVO 40 microscope featuring a tungsten cathode and a lithium-drifted silicon detector. For TEM, SnO₂/Fe₂O₃/IrO₂ nanotubes were dissolved in 0.1 M NaOH and characterized using a JEOL 3010 microscope. The crystal structure was investigated by powder X-ray diffraction measurements using a Bruker D8 Advance diffractometer in reflection mode and with Cu Kα₁ radiation (λ = 1.54056 Å) and LynxEye XE-T detector. A polynomial

baseline correction was applied. Monochromatized Al K α XPS spectra were acquired on a PHI Quantera II system with a base pressure of 1×10^{-9} mbar. A combination of electron and ion neutralization was employed to prevent charging. The Sn 3d, Fe 2p, O 1s, and Ir 4f XPS core level spectra were analyzed using a fitting routine that decomposes each spectrum into individual mixed Gaussian–Lorentzian peaks using a Shirley background subtraction over the energy range of the fit. Finally, all spectra were shifted to yield a C 1s binding energy position of 284.8 eV. The loading of the IrO₂ cocatalyst was determined by ICP-OES (Optima 8300, Perkin Elmer). For the ICP-OES analysis, four-point calibrations (50, 10, 1, and 0.1 ppm) were performed by diluting certified standards. Samples were measured in triplicate and mean values were reported.

Electrochemical Studies: The nanostructured electrodes were laser-cut with a GCC LaserPro Spirit LS Laser into circular pieces and glued with the nickel contact on small copper plates using double-sided conductive copper foil. The sample area exposed to the electrolyte was defined by a chemically resistant and electrically insulating polyimide (Kapton) adhesive tape featuring a laser-cut circular window of 2.0 mm diameter. This macroscopically defined sample area $A = 0.031 \text{ cm}^2$ was used to define current densities $J = I/A$ from the measured currents I . The samples were then adjusted into three-electrode electrochemical cells with a Pt mesh as counter electrode and a Ag/AgCl/KCl (sat.) reference electrode (standard redox potential shifted by +0.20 V relative to the NHE). All electrochemical measurements including cyclic voltammetry, EIS, and steady-state electrolysis were done at room temperature in a 0.1 M KH₂PO₄ electrolyte adjusted to pH 7 or 1 M NaOH using a Gamry Reference 600 or Gamry Interface 1000 potentiostat. Cyclic voltammograms were measured at a scan rate of 10 mV s⁻¹. Impedance data were collected between 100 kHz and 0.05 Hz at +1.10 V applied potential using 10 mV amplitude perturbation and analyzed with Gamry Echem Analyst in order to generate the fits presented. Steady-state electrolysis measurements were carried out in a potential range of +1.30 V \geq $E \geq$ +0.90 V (overpotentials $0.68 \geq \eta \geq 0.28$ V) each for 3 h. The current densities J presented in the main text are mean values of the last hour of electrolysis, averaged over at least three individual electrodes. Cyclic voltammetry and chronoamperometry under light-chopping conditions were performed with a solar simulator (AM 1.5G) from Newport Model 69907 with a 15 W Xe lamp. The light intensity was calibrated to 100 mW cm⁻² with a reference Si solar cell.

Supporting Information

Supporting Information is available from the Wiley Online Library or from the author.

Acknowledgements

The authors thank A. Both-Engel for the XPS measurements. The authors further acknowledge Prof. W. Peukert and P. Hoppe for the ICP-OES data. This work was funded in part by the project “tubulAir \pm ” (No. 03SF0436G) supported by the Bundesministerium für Bildung und Forschung, by the European Research Council (ERC) under the European Union’s Horizon 2020 research and innovation program (Grant Agreement No. 647281, “Solacylin”), and by COST Action MP1402 “HERALD”, a European cooperation program. M.E.D. is indebted to the French Ministry of Higher Education, Research and Innovation for the Ph.D. grant.

Conflict of Interest

The authors declare no conflict of interest.

Keywords

atomic layer deposition, iridium oxide, iron oxide, nanostructures, water splitting

Received: September 16, 2018

Revised: November 10, 2018

Published online: December 3, 2018

- [1] N. S. Lewis, D. G. Nocera, *Proc. Natl. Acad. Sci. USA* **2006**, *103*, 15729.
- [2] a) O. Zandi, T. W. Hamann, *Phys. Chem. Chem. Phys.* **2015**, *17*, 22485; b) E. Fabbri, A. Habereder, K. Waltar, R. Kötter, T. J. Schmidt, *Catal. Sci. Technol.* **2014**, *4*, 3800.
- [3] K. Sivula, F. Le Formal, M. Grätzel, *ChemSusChem* **2011**, *4*, 432.
- [4] T. R. Cook, D. K. Dogutan, S. Y. Reece, Y. Surendranath, T. S. Teets, D. G. Nocera, *Chem. Rev.* **2010**, *110*, 6474.
- [5] J. W. Morgan, E. Anders, *Proc. Natl. Acad. Sci. USA* **1980**, *77*, 6973.
- [6] a) J. K. Leland, A. J. Bard, *J. Phys. Chem.* **1987**, *91*, 5076; b) K. L. Hardee, A. J. Bard, *J. Electrochem. Soc.* **1976**, *123*, 1024; c) T. Lindgren, L. Vayssieres, H. Wang, S.-E. Lindquist, in *Chemical Physics of Nanostructured Semiconductors* (Eds: A. I. Kokorin, D. W. Bahnemann), VSP International Science Publishers, Zeist, The Netherlands **2003**, Ch. 3.
- [7] a) M. Grätzel, *Nature* **2001**, *414*, 338; b) A. G. Tamirat, J. Rick, A. A. Dubale, W.-N. Su, B.-J. Hwang, *Nanoscale Horiz.* **2016**, *1*, 243.
- [8] N. Takeno, *Atlas of Eh–pH Diagrams, Intercomparison of Thermodynamic Databases, Geological Survey of Japan Open File Report No. 419*, National Institute of Advanced Industrial Science and Technology, Research Center for Deep Geological Environments, Tsukuba, Japan **2005**.
- [9] M. P. Dare-Edwards, J. B. Goodenough, A. Hamnett, P. R. Trelvelick, *J. Chem. Soc., Faraday Trans. 1* **1983**, *79*, 2027.
- [10] F. J. Morin, *Phys. Rev.* **1951**, *83*, 1005.
- [11] J. R. Bolton, S. J. Strickler, J. S. Connolly, *Nature* **1985**, *316*, 495.
- [12] J. H. Kennedy, K. W. Frese, *J. Electrochem. Soc.* **1978**, *125*, 709.
- [13] a) U. Joerksten, J. Moser, M. Graetzel, *Chem. Mater.* **1994**, *6*, 858; b) T. Lindgren, H. Wang, N. Beermann, L. Vayssieres, A. Hagfeldt, S.-E. Lindquist, *Sol. Energy Mater. Sol. Cells* **2002**, *71*, 231.
- [14] a) A. Kay, I. Cesar, M. Grätzel, *J. Am. Chem. Soc.* **2006**, *128*, 15714; b) N. Beermann, L. Vayssieres, S.-E. Lindquist, A. Hagfeldt, *J. Electrochem. Soc.* **2000**, *147*, 2456; c) N. T. Hahn, H. Ye, D. W. Flaherty, A. J. Bard, C. B. Mullins, *ACS Nano* **2010**, *4*, 1977.
- [15] a) F. E. Osterloh, *Chem. Soc. Rev.* **2013**, *42*, 2294; b) T. W. Hamann, *Dalton Trans.* **2012**, *41*, 7830; c) B. M. Klahr, A. B. F. Martinson, T. W. Hamann, *Langmuir* **2011**, *27*, 461; d) S. C. Riha, M. J. DeVries Vermeer, M. J. Pellin, J. T. Hupp, A. B. F. Martinson, *ACS Appl. Mater. Interfaces* **2013**, *5*, 360.
- [16] a) K. Sivula, F. Le Formal, M. Grätzel, *Chem. Mater.* **2009**, *21*, 2862; b) A. Müller, I. Kondofersky, A. Folger, D. Fattakhova-Rohlfing, T. Bein, C. Scheu, *Mater. Res. Express* **2017**, *4*, 016409; c) Y. Lin, S. Zhou, S. W. Sheehan, D. Wang, *J. Am. Chem. Soc.* **2011**, *133*, 2398; d) M. Stefiik, M. Cornuz, N. Mathews, T. Hisatomi, S. Mhaisalkar, M. Grätzel, *Nano Lett.* **2012**, *12*, 5431.
- [17] a) S. D. Tilley, M. Cornuz, K. Sivula, M. Grätzel, *Angew. Chem., Int. Ed.* **2010**, *49*, 6405; b) L. Badi-Bou, E. Mas-Marza, P. Rodenas, E. M. Barea, F. Fabregat-Santiago, S. Gimenez, E. Peris, J. Bisquert, *J. Phys. Chem. C* **2013**, *117*, 3826; c) G. M. Carroll, D. R. Gamelin, *J. Mater. Chem. A* **2016**, *4*, 2986; d) D. K. Zhong, D. R. Gamelin, *J. Am. Chem. Soc.* **2010**, *132*, 4202; e) Y.-R. Hong, Z. Liu, S. F. B. S. A. Al-Bukhari, C. J. J. Lee, D. L. Yung, D. Chi, T. S. A. Hor, *Chem. Commun.* **2011**, *47*, 10653.
- [18] G. G. Bessegato, T. T. Guaraldo, J. Ferreira de Brito, M. F. Brugnera, M. V. B. Zanoni, *Electrocatalysis* **2015**, *6*, 415.

- [19] a) D. Jousse, C. Constantino, I. Chambouleyron, *J. Appl. Phys.* **1983**, 54, 431; b) A. F. Khan, M. Mehmood, A. M. Rana, M. T. Bhatti, *Appl. Surf. Sci.* **2009**, 255, 8562; c) S. Muranaka, Y. Bando, T. Takada, *Thin Solid Films* **1981**, 86, 11.
- [20] S. Trasatti, *Electrochim. Acta* **1984**, 29, 1503.
- [21] a) E. Rasten, G. Hagen, R. Tunold, *Electrochim. Acta* **2003**, 48, 3945; b) Y. Wang, D. Y. C. Leung, J. Xuan, H. Wang, *Renewable Sustainable Energy Rev.* **2017**, 75, 775; c) M. G. Chourashiya, A. Urakawa, *J. Mater. Chem. A* **2017**, 5, 4774.
- [22] a) J. Gemmer, Y. Hinrichsen, A. Abel, J. Bachmann, *J. Catal.* **2012**, 290, 220; b) S. Haschke, Y. Wu, M. Bashouti, S. Christiansen, J. Bachmann, *ChemCatChem* **2015**, 7, 2455; c) S. Haschke, D. Pankin, Y. Petrov, S. Bochmann, A. Manshina, J. Bachmann, *ChemSusChem* **2017**, 10, 3644.
- [23] M. K. S. Barr, L. Assaud, N. Brazeau, M. Hanbücken, S. Ntais, L. Santinacci, E. A. Baranova, *J. Phys. Chem. C* **2017**, 121, 17727.
- [24] a) X. Meng, J. Yao, F. Liu, H. He, M. Zhou, P. Xiao, Y. Zhang, *J. Alloys Compd.* **2013**, 552, 392; b) Q. Tian, Z. Zhang, L. Yang, S.-i. Hirano, *J. Power Sources* **2014**, 253, 9.
- [25] a) T. Fujii, F. M. F. de Groot, G. A. Sawatzky, F. C. Voogt, T. Hibma, K. Okada, *Phys. Rev. B* **1999**, 59, 3195; b) N. S. McIntyre, D. G. Zetaruk, *Anal. Chem.* **1977**, 49, 1521.
- [26] L. Steier, J. Luo, M. Schreier, M. T. Mayer, T. Sajavaara, M. Grätzel, *ACS Nano* **2015**, 9, 11775.
- [27] S. Schlicht, S. Haschke, V. Mikhailovskii, A. Manshina, J. Bachmann, *ChemElectroChem* **2018**, 5, 1259.
- [28] a) S. J. Freakley, J. Ruiz-Esquiús, D. J. Morgan, *Surf. Interface Anal.* **2017**, 49, 794; b) R.-S. Chen, Y.-S. Huang, Y.-M. Liang, D.-S. Tsai, Y. Chi, J.-J. Kai, *J. Mater. Chem.* **2003**, 13, 2525.
- [29] a) A. Irshad, N. Munichandraiah, *RSC Adv.* **2017**, 7, 21430; b) A. Minguzzi, F.-R. F. Fan, A. Vertova, S. Rondinini, A. J. Bard, *Chem. Sci.* **2012**, 3, 217; c) P. Steegstra, E. Ahlberg, *Electrochim. Acta* **2012**, 76, 26; d) A. A. F. Grupioni, E. Arashiro, T. A. F. Lassali, *Electrochim. Acta* **2002**, 48, 407.
- [30] S. Rühle, *Sol. Energy* **2016**, 130, 139.
- [31] a) Y. Sun, W. D. Chemelewski, S. P. Berglund, C. Li, H. He, G. Shi, C. B. Mullins, *ACS Appl. Mater. Interfaces* **2014**, 6, 5494; b) S. Park, H. J. Kim, C. W. Lee, H. J. Song, S. S. Shin, S. W. Seo, H. K. Park, S. Lee, D.-W. Kim, K. S. Hong, *Int. J. Hydrogen Energy* **2014**, 39, 16459; c) L. Wang, A. Palacios-Padrós, R. Kirchgeorg, A. Tighineanu, P. Schmuki, *ChemSusChem* **2014**, 7, 421.
- [32] Y. F. Xu, H. S. Rao, B. X. Chen, Y. Lin, H. Y. Chen, D. B. Kuang, C. Y. Su, *Adv. Sci.* **2015**, 2, 1500049.
- [33] H. Masuda, K. Fukuda, *Science* **1995**, 268, 1466.